Chapter 3

A hyperthermal O-atom exchange reaction, O_2 + CO_2

Adapted from Yeung, L. Y., M. Okumura, J. T. Paci, G. C. Schatz, J. Zhang, and T. K. Minton (2009), Hyperthermal O-Atom Exchange Reaction O_2 + CO_2 through a CO_4 Intermediate, *J. Am. Chem. Soc.*, *131*(39): 13,940–13,942.

3.1 Abstract

O_2 and CO_2 do not react under ordinary conditions, owing to the thermodynamic stability of CO_2 and the large activation energy required for multiple double-bond cleavage. We present evidence for a gas-phase O-atom exchange reaction between neutral O_2 and CO_2 at elevated collision energies ($\approx$ 160 kcal mol^{-1}) from crossed-molecular-beams experiments. Products were scattered mainly in the forward direction, i.e., in the initial direction of the hyperthermal oxygen beam in the center-of-mass (c.m.) frame, with 16% of the available energy in translation, on average. CCSD(T)/aug-cc-pVTZ calculations demonstrate that isotope exchange can occur on the ground triplet potential energy surface through a short-lived CO_4 intermediate that isomerizes via a symmetric CO_4 transition state containing a bridging oxygen atom. We propose a plausible adiabatic mechanism for this reaction supported by additional spin-density calculations.

3.2 Introduction

O_2 and CO_2 do not react under ordinary conditions. This can be attributed to the large activation energy for multiple double-bond cleavage, as Dixon illustrated in his early experiments in which dry CO–O_2–CO_2 mixtures "did not explode" when subjected to a spark discharge [*Dixon*, 1886]. *Otomo et al.* [2000] later reported a reaction of CO_2 and electronically excited O_2^* when they observed O_3 products after irradiating super- and sub-critical O_2/CO_2 mixtures with UV light. While investigating the isotope exchange reaction

$$^{16}O(^3P) + {}^{12}C{}^{18}O_2 \rightarrow {}^{18}O + {}^{16}O{}^{12}C{}^{18}O \tag{3.1}$$

at hyperthermal collision energies in a crossed-molecular-beams experiment, we found evidence for the gas-phase oxygen isotope exchange reaction

$$^{16}O_2 + {}^{12}C{}^{18}O_2 \rightarrow {}^{18}O{}^{16}O + {}^{16}O{}^{12}C{}^{18}O \tag{3.2}$$

of ground-state reactants at high collision energies ($\sim$160 kcal mol^{-1}). Our observations on the dynamics of this reaction, taken together with *ab initio* calculations of stationary points on the lowest triplet potential energy surface (PES), suggest a plausible adiabatic mechanism for the reaction of O_2 with CO_2 through a CO_4 transition complex.

3.3 Experimental studies

3.3.1 Methods

Crossed-molecular-beam experiments were performed with a hyperthermal oxygen source containing $\sim$87% O(^3P) and $\sim$13% $O_2(^3\Sigma_g^-)$ [*Brunsvold et al.*, 2007, 2008; *Garton et al.*, 2006, 2009]. A diagram of the experimental setup, configured for $^{16}O(^3P)$ + $^{12}C^{18}O_2$ collisions, is shown in Figure 3.1. A pulsed beam of $^{16}O(^3P)$ and $^{16}O_2$ ($^3\Sigma_g^+$; at an unknown vibrational temperature) was generated by laser-induced detonation of $^{16}O_2$ using a high-energy CO_2 TEA laser (6 – 7 J pulse^{-1}) operating at a pulse repetition rate of 2 Hz. Though initially broad in velocity distribution (6 – 9 km s^{-1}), a portion of the overall

beam was velocity-selected for the scattering experiments using a synchronized chopper wheel operating at 300 Hz. This velocity-selected beam was crossed, at a nominal angle of 90°, with a pulsed supersonic expansion of 98% $^{12}C^{18}O_2$ gas (2% $^{16}O^{12}C^{18}O$; Spectra Gas). The molecular beams and scattered products were detected with a rotatable quadrupole mass spectrometer with electron-bombardment ionization [*Brink*, 1966] at 160 eV and a Daly-type ion counter [*Daly*, 1960]. $^{12}C^{18}O_2$ and $^{16}O^{12}C^{18}O$ products were detected at m/z = 48 ($^{12}C^{18}O_2^+$) and 46 ($^{16}O^{12}C^{18}O^+$), respectively, with a rotatable mass spectrometer that collected number density distributions as a function of arrival time, $N(t)$, at a given laboratory angle, Θ, using a multi-channel plate (MCP). Here, Θ is defined as the angle at which the $^{16}O^{12}C^{18}O$ scatters with respect to the direction of the reagent oxygen beam (i.e., Θ = 0°). Time-of-flight (TOF) distributions for $^{16}O(^3P)$, $^{16}O_2$, $^{12}C^{18}O_2$, and $^{16}O^{12}C^{18}O$ were collected over a range of laboratory angles (6° – 54°); at each angle, the TOF distribution for the 33.7-cm distance between the beam interaction region to the ionizer was integrated to give a laboratory angular distribution, $N(\Theta)$. A forward-convolution method was used to derive the center-of-mass (c.m.) translational energy $P(E_T)$ and angular $T(\theta_{c.m.})$ distributions from the laboratory $N(t)$ and $N(\Theta)$ distributions [*Lee*, 1988], where $\theta_{c.m.}$ is the angle at which $^{16}O^{12}C^{18}O$ scatters with respect to the reagent oxygen direction in the c.m. frame. The canonical Newton diagrams used in this analysis are shown in Figure 3.2.

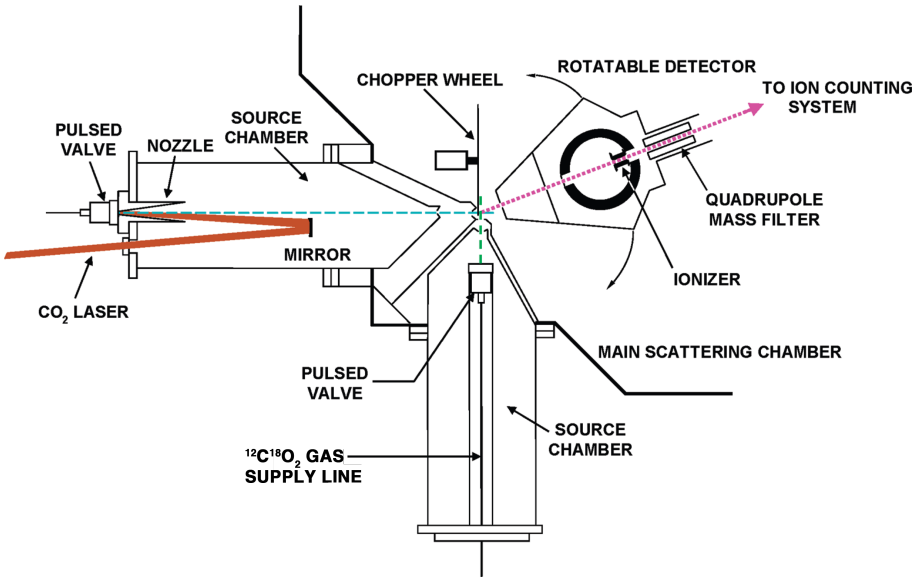

Figure 3.1: **Crossed-molecular-beam apparatus with hyperthermal oxygen source.**

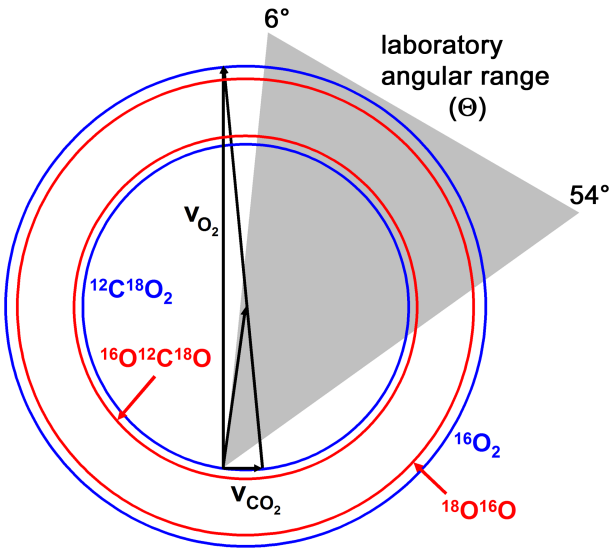

Figure 3.2: **Canonical Newton diagram for hyperthermal $^{16}O_2$ + $^{12}C^{18}O_2$ collisions.** The Newton circles represent the maximum recoil velocities of the products.

The hyperthermal oxygen beam was generated by laser detonation of a pulsed expansion of O_2 gas with 500 psig stagnation pressure using a source based on the design of *Caledonia et al.* [1987]. 174 μs after the pulsed valve is triggered, the CO_2 laser is fired; the laser pulse passed through an antireflection-coated ZnSe window in to the source chamber, whereupon it was reflected back towards the gold-plated, water-cooled copper nozzle with a 1 m radius concave gold mirror. The focused laser pulse initiates a breakdown of the O_2 gas and heats the resulting plasma to $>$ 20,000 K, which accelerates both the atomic and molecular oxygen fractions of the pulsed beam to 6 – 9 km s^{-1}. Use of a conical nozzle allowed for efficient ion-electron recombination and inefficient atom-atom and atom-molecule recombination as the plasma expanded and cooled. The resulting gas pulse was collimated by a 1 cm diameter aperture located 80 cm downstream of the inlet nozzle into a differentially pumped region (10^{-5} – 10^{-6} Torr), after which it passed through a 1.2-mm-diameter skimmer 16 cm further downstream. The beam interaction region was an additional 3 cm downstream in the main chamber (2×10^{-7} Torr), a total distance of 99 cm from the inlet nozzle.

For velocity selection within the hyperthermal oxygen beam, a chopper wheel running at 300 Hz (synchronized with the 2-Hz laser pulses) was placed inside the main scattering

chamber, just downstream of the skimmer. Three equally-spaced slots (1.5 mm wide) of the chopper wheel pass over an LED/photodiode assembly a quarter-turn before each slot enters the beam axis, generating a 900 Hz (3 $\times$ 300 Hz) train of pulses. These chopper wheel pulses are sent to a digital delay generator and used as references for triggering the O_2 gas pulses. The time delay between the chopper wheel pulse and the O_2 pulse determined the portion of the overall hyperthermal oxygen beam allowed to pass through into the interaction region.

We characterized the velocity distribution of the hyperthermal oxygen beam under two conditions: on axis ($\Theta = 0^\circ$) with a small aperture ($\sim$125 μm diameter) to obtain the peak of the distribution, and off axis ($\Theta = 3^\circ$) with a large aperture (4 mm $\times$ 4 mm) to obtain the width of the distribution. For the on-axis configuration, a 2 mA emission current at the ionizer and a –18 kV potential at the secondary emitting electrode of the Daly ion counter was used. For the off-axis configuration, a 10 mA emission current at the ionizer and a –30 kV potential at the secondary emitting electrode was used. Laboratory TOF distributions under both conditions were measured, for both ^{16}O and $^{16}O_2$, to determine the laboratory-frame velocities and translational energy distributions for the hyperthermal oxygen beam. In these experiments, the average velocity of the hyperthermal oxygen beam was thus determined to be 8262 $\pm$ 450 m s^{-1} (i.e., 900 m s^{-1} full width at half maximum; FWHM), which corresponds to average translational energies $\langle E_T \rangle$ = 130.5 $\pm$ 14 kcal mol^{-1} and 261.0 $\pm$ 28 kcal mol^{-1} FWHM for $^{16}O(^3P)$ and $^{16}O_2$, respectively (see Figure 3.3). The relative amounts of atomic ($\sim$87%) and molecular ($\sim$13%) oxygen were determined by integrating the TOF distributions at m/z = 16 ($^{16}O^+$) and 32 ($^{16}O_2{}^+$) at $\Theta = 0^\circ$ and correcting for O_2 fragmentation (11% of the m/z = 32 signal) in the electron-bombardment ionization region.

A pulsed supersonic expansion of $^{12}C^{18}O_2$ was generated using a piezoelectric pulsed general valve with a 1300-Torr stagnation pressure. The expansion passed through a 2 mm diameter skimmer (9.2 cm from the nozzle) into a differential pumping region, and then through a 2.5 mm diameter (2.8 cm downstream of the skimmer) aperture into the main scattering chamber. The distance from this aperture to the interaction region was 1.5 cm.

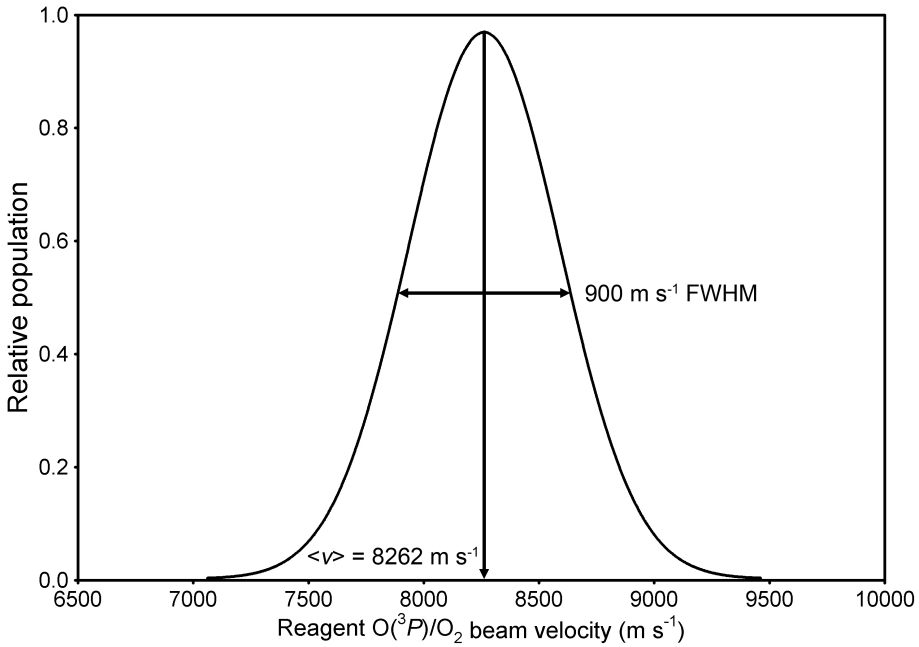

Figure 3.3: **Velocity distribution of hyperthermal oxygen beam.**

The velocity distribution of the $^{12}C^{18}O_2$ beam was not measured directly, and instead was determined iteratively by first estimating the terminal velocity of the supersonic expansion [*Lee*, 1988] and then fitting the $^{12}C^{18}O_2$ velocity to the value that yielded the best Newton circle for non-reactively scattered O-atoms while keeping the measured O-atom velocity distribution fixed at its measured values. This contributes some uncertainty to the measured TOF distributions because the $^{12}C^{18}O_2$ beam velocity is likely only accurate to $\pm$10%. However, because the magnitude of the hyperthermal oxygen beam velocity at the interaction region was ten times that of the $^{12}C^{18}O_2$ beam, and its FWHM was also 4 – 5 times that of the $^{12}C^{18}O_2$ beam, uncertainties in the "time-zero" of the hyperthermal oxygen source dominated the overall uncertainty in the measured translational energy distributions.

Laboratory TOF product distributions were measured every 2° between Θ = 6° – 54°. Scattered product TOF distributions were collected for 200 beam pulses for for m/z = 16 ($^{16}O^+$) and 32 ($^{16}O_2{}^+$), for 1000 beam pulses for m/z = 46 ($^{16}O^{12}C^{18}O^+$), and for 500 beam pulses for m/z = 48 ($^{12}C^{18}O_2{}^+$). Dwell time for each channel at the MCP was 1 μs. At a representative laboratory angle of 10°, integrated count rates were 1.1 $\times$ 10^7 s^{-1} for m/z = 16, 1.3 $\times$ 10^7 s^{-1} for m/z = 32, 1.8 $\times$ 10^5 s^{-1} for m/z = 46 , and 4.2 $\times$ 10^6 s^{-1} for m/z

= 48. Raw flight times were converted to flight times over the 33.7 cm distance between the interaction region and the electron-bombardment ionizer by subtracting the O_2 trigger-pulse-to-laser-fire delay time (174 μs), an electronic-latency delay time (3 μs), the oxygen flight time from the nozzle to the interaction region (120 μs, corresponding to the average velocity of the hyperthermal oxygen beam), and finally the ion flight time between the ionizer and the Daly ion counter. The ion flight time is given by $\alpha(m/z)^{\frac{1}{2}}$, where $\alpha = 2.44$ in these experiments, determined by comparing the relative arrival times of hyperthermal ^{16}O and $^{16}O_2$ at the detector [*Garton et al.*, 2006]. Some uncertainty arises in the product times-of-flight because the exact time- and point-of-origin of the hyperthermal oxygen beam are not well determined; we estimate this uncertainty to be $\sim$2 μs because the laser pulse width in the hyperthermal oxygen source could be as long as 1 μs (a 100 ns-wide peak with a slow tail).

Two signal corrections were made before data analysis. First, we corrected for beam divergence at $\Theta = 6^\circ - 16^\circ$. The divergent intensity with the $^{12}C^{18}O_2$ beam turned off was measured by obtaining TOF distributions at $m/z = 16$ and 32 from $\Theta = 6^\circ - 16^\circ$. These TOF distributions were then scaled and subtracted from the corresponding experimental TOF distributions at $m/z = 16$ and 32 that had the $^{12}C^{18}O_2$ beam turned on. Uncertainties in the inelastic and reactive scattering signals due to collisions of the divergent hyperthermal oxygen could not quantified, however; they were instead considered in the analysis of the laboratory data, where collisions at crossing angles of 88°, 89°, 90°, 91°, and 92° were included during forward-convolution fitting. Adding more crossing angles did not affect the forward-convolution fits significantly. Second, we verified that the $^{12}C^{18}O_2$ beam contained 2% $^{16}O^{12}C^{18}O$ using the instrument's mass spectrometer. Thus, 2% of the inelastic scattering signal ($m/z = 48$) at each laboratory angle ($\Theta = 6^\circ - 54^\circ$) was subtracted from raw $m/z = 46$ ($^{16}O^{12}C^{18}O^+$) TOF distributions to obtain reactive-scattering-only distributions.

A forward-convolution method was employed to perform the laboratory-to-c.m. frame coordinate transformation [*Lee*, 1988] of the data using the MSU XBEAM program (Version 6). Trial $P(E_T)$ and $T(\theta_{c.m.})$ distributions were used to simulate the laboratory-frame TOF distributions using the following relationship derived from the Jacobian transformation:

$$N(t,\Theta)\ \alpha\ \frac{l^3}{ut^3}P(E_{\mathrm{T}})T(\theta_{\mathrm{c.m.}}) \tag{3.3}$$

where l and t are the distance and flight time, respectively, from the interaction region to the ionizer, and u is the product velocity in the c.m. frame. During the fitting process, $^{12}C^{18}O_2$ was assumed to have a single-valued velocity, 800 m s^{-1}, because the large magnitude and width of the hyperthermal oxygen beam velocity distribution is principally responsible (i.e., it contributed $\geq$ 98% of the uncertainty in the c.m. collision energy; see above) for the observed width of the laboratory TOF distributions and the c.m. translational energy distributions. The width of the hyperthermal beam velocity distribution was fit by a Gaussian function centered at 8262 m s^{-1} and a FWHM of 900 m s^{-1}, which was used during data analysis. Note that the data we report for flight times over a 33.7 cm distance were calculated by subtracting the *average* oxygen flight time from the nozzle to the interaction region; the reported product arrival times, then, reflect a convolution of the oxygen beam's wide velocity distribution and the 'true' product translational energy distribution, so the best-fit $P(E_{\mathrm{T}})$ distributions may not be unique. As such, we estimate the uncertainties in the reported $P(E_{\mathrm{T}})$ distribution to be 10 – 20%.

To allow for easy manipulation of the $P(E_{\mathrm{T}})$ and $T(\theta_{\mathrm{c.m.}})$ distributions, parameterized functions were often used. The fitting process often relied on the RRK form of the $P(E_{\mathrm{T}})$ distribution:

$$P(E_{\mathrm{T}})\ =\ (E_{\mathrm{T}}\ -\ B)^p(E_{\mathrm{avail}}\ -\ E_{\mathrm{T}})^q \tag{3.4}$$

where E_{avail} is the available translational energy in the c.m. frame (i.e., the collision energy, E_{coll}, minus the endothermicity, ΔE). The parameters B, p, and q were adjusted to vary the peak and width of the c.m. translational energy distribution when obtaining a best fit to the laboratory data. The $T(\theta_{\mathrm{c.m.}})$ distribution was described by a Legendre polynomial form:

$$T_k(\theta_{\mathrm{c.m.}})\ =\ \frac{a_k}{2^k k!}\frac{c^k(\cos^2\theta_{\mathrm{c.m.}}\ -\ 1)^k}{c(\cos\theta_{\mathrm{c.m.}})} \tag{3.5}$$

where a_k is an adjustable parameter for each of the eleven polynomial terms used, which

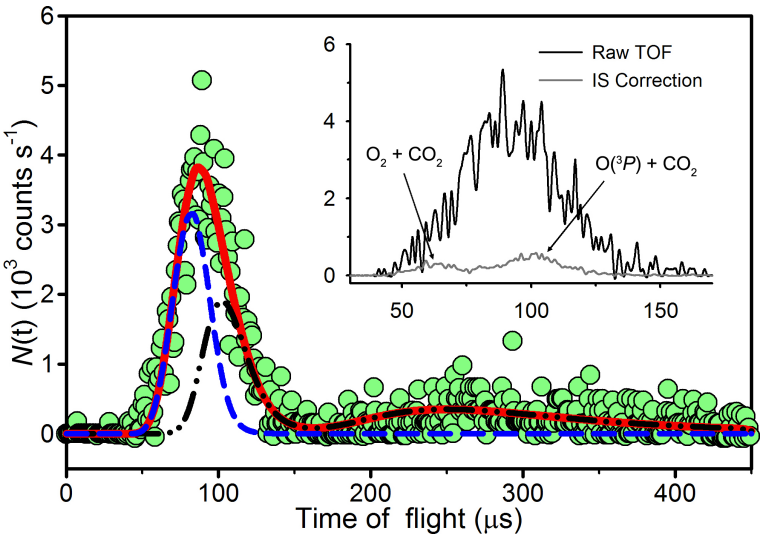

Figure 3.4: **Laboratory TOF distribution of m/z = 46 ($^{16}O^{12}C^{18}O^+$; green circles) at Θ = 6°, with the inelastic scattering signal removed.** The data are shown with the $O(^3P)$ + CO_2 (dot-dashed black line), O_2 + CO_2 (dashed blue line), and summed (solid red line) forward-convolution fits. Flight times less than 72 μs violate energy conservation for $^{16}O(^3P)$ + $^{12}C^{18}O_2$. The inset compares the raw TOF distribution with the IS TOF distribution, which is subtracted.

were denoted by the subscripted k = 0, 1, 2,...10. The functional forms for the $P(E_T)$ and $T(\theta_{c.m.})$ distributions (3.4 and 3.5, respectively), were iterated in XBEAM until they provided satisfactory fits to the laboratory data, though, in some cases, point forms of the $P(E_T)$ and $T(\theta_{c.m.})$ distributions were used. Finally, the "best-fit" $P(E_T)$ and $T(\theta_{c.m.})$ distributions were used to create a c.m. velocity-flux contour map or a differential scattering cross-section plot for the products.

3.3.2 Results

The inset in Figure 3.4 shows a raw m/z = 46 TOF distribution of $^{16}O^{12}C^{18}O$ products recorded at Θ = 6°. A small fraction of the signal can be attributed to inelastic scattering (IS) of $^{16}O^{12}C^{18}O$ impurities in the CO_2 beam by ^{16}O and $^{16}O_2$, and it can be subtracted. The remaining signal, shown in Figure 3.4, represents $^{16}O^{12}C^{18}O$ products from O-atom exchange reactions of $^{12}C^{18}O_2$ (see Chapter 4).

We initially expected the reactive m/z = 46 signal to arise from reactions of $^{12}C^{18}O_2$ with the ^{16}O atoms (reaction 3.1) with a broad distribution of c.m. collision energies (E_{coll})

peaked at 98.8 kcal mol^{-1} and a full width at half maximum (FWHM) of 18 kcal mol^{-1}. However, at small laboratory angles, we observed products with velocities that would violate energy conservation for this O(^3P) + CO_2 reaction (e.g., t $<$ 72 μs in Figure 3.4). $^{12}C^{18}O_2$ was estimated to have a laboratory velocity of 800 $\pm$ 80 m s^{-1} (see *Lee* [1988]). Given the broad velocity distribution in the O(^3P)/O_2 beam (8262 m s^{-1} with 900 m s^{-1} FWHM), the velocity spread in the $^{12}C^{18}O_2$ beam was insignificant by comparison, so the hyperthermal oxygen beam largely determined the broad distribution of collision energies sampled in these experiments. To calculate the maximum available translational energy in the laboratory frame for ^{16}O(^3P) + $^{12}C^{18}O_2$ and $^{16}O_2$ + $^{12}C^{18}O_2$ isotope exchange reactions, an initial ^{16}O(^3P)/$^{16}O_2$ beam velocity of 8862 m s^{-1} was used because $<$ 5% of the O(^3P)/O_2 beam had a greater velocity. A non-negligible population of $^{16}O^{12}C^{18}O$ was observed at translational energies above the maximum allowed for ^{16}O(^3P) + $^{12}C^{18}O_2$ collisions at small laboratory angles.

Despite the uncertainties in the E_{coll} distribution and product flight times (see Section 3.3.1), we observed $^{16}O^{12}C^{18}O$ products arrive 10 – 20 μs faster than the minimum times allowed by the distribution of available energies, E_{avail} ($\approx E_{coll}$; the zero-point energy change is +0.1 kcal mol^{-1}), for reaction 3.1. Forward-convolution best-fits to the TOF distributions that only treat the ^{16}O(^3P) + $^{12}C^{18}O_2$ isotope exchange reaction cannot explain the fastest laboratory data at small laboratory angles (e.g., $\Theta = 6^\circ$ and 8°; see Figure 3.5). Increasing $\langle E_T \rangle$ in the product $P(E_T)$ shifts the fastest part of the fit towards shorter flight times at all laboratory angles. While this improves the TOF fits at small laboratory angles, it decreases the quality of the TOF fits at larger laboratory angles (see $\Theta = 36^\circ$ in Figure 3.6). Introducing the $^{16}O_2$ + $^{12}C^{18}O_2$ isotope exchange reaction yields good fits at all laboratory angles. A sizeable fraction of the products assigned to the $^{16}O_2$ + $^{12}C^{18}O_2$ reaction are slow enough that they do not violate conservation of energy; however, assigning them to the ^{16}O(^3P) + $^{12}C^{18}O_2$ reaction leads to poor fits. Collisions between CO_2 and ions or electronically excited O atoms could also yield $^{16}O^{12}C^{18}O$ products with elevated velocities, previous experience with this hyperthermal source indicates that they are not present in the beam [*Troya et al.*, 2004].

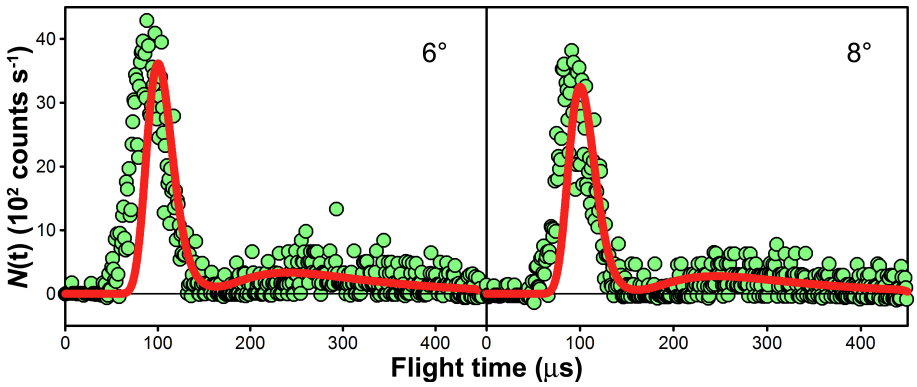

Figure 3.5: **TOF distributions (green dots) for $^{16}O^{12}C^{18}O$ products at laboratory angles $\Theta = 6^\circ$ and 8° with the inelastic scattering signal removed.** Also shown are forward-convolution best fits (solid red line) that treat only one isotope exchange reaction, $^{16}O(^3P)$ + $^{12}C^{18}O_2$ → O + $^{12}C^{18}O_2$. The forward-convolution fits cannot account for the fastest $^{16}O^{12}C^{18}O$ product signals at small laboratory angles.

We therefore hypothesize that the fast $^{16}O^{12}C^{18}O$ products come from reaction of $^{12}C^{18}O_2$ with $^{16}O_2$ in the hyperthermal beam. Because the velocity-selected $^{16}O_2$ molecules have the same laboratory-frame velocity distribution as the ^{16}O atoms, the $^{16}O_2$ molecules collide with the $^{12}C^{18}O_2$ molecules at substantially higher c.m. energies (see Newton diagram in Figure 3.2). The resulting collision energy distribution peaked at E_{coll} = 158 kcal mol^{-1} with FWHM = 28 kcal mol^{-1}. Thus, $^{16}O^{12}C^{18}O$ products from reaction 3.2 have sufficient E_{avail} to account for the fastest products detected. The m/z = 46 signal would then contain products of both reactions 3.1 and 3.2, the fastest products arising exclusively from reaction 3.2.

$P(E_T)$ and $T(\theta_{c.m.})$ distributions for reactions 3.1 and 3.2 were simultaneously obtained from forward-convolution fits of the m/z = 46 TOF distributions. The results for the $^{16}O_2$ + $^{12}C^{18}O_2$ reaction are presented in Figure 3.7; a c.m. velocity-flux contour diagram of $^{16}O^{12}C^{18}O$ products is shown in Figure 3.8, in which the observed product flux is peaked in the forward direction. The presence of signal at flight times violating energy conservation for $^{16}O(^3P)$–$^{12}C^{18}O_2$ collisions was used to guide the fitting process because the TOF distributions do not resolve the products unambiguously. As such, we cannot rule out an additional dynamical channel in reaction 3.1 contributing to some of the signal we attribute to reaction 3.2 because energy conservation in reaction 3.1 is only violated at small lab angles.

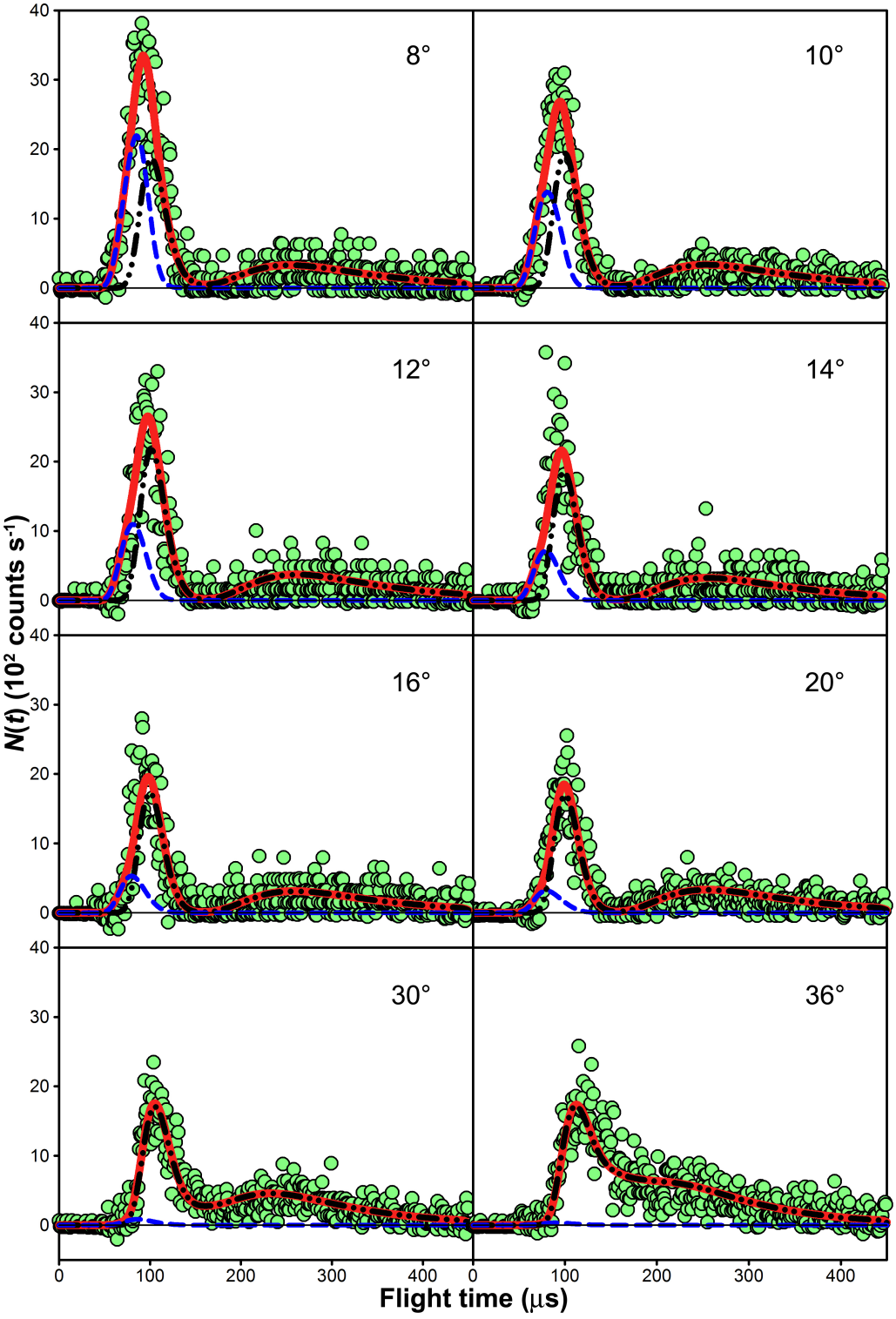

Figure 3.6: **TOF distributions for $^{16}O^{12}C^{18}O$ (m/z = 46) at various laboratory angles Θ with the inelastic scattering signal removed.** The raw data are shown as circles. Forward-convolution fits of the $^{16}O_2$ + $^{12}C^{18}O_2$ (blue dashed curve) and $^{16}O(^3P)$ + $^{12}C^{18}O_2$ (black dot-dashed dashed curve) channels, along with their sum (red solid curve), are also shown.

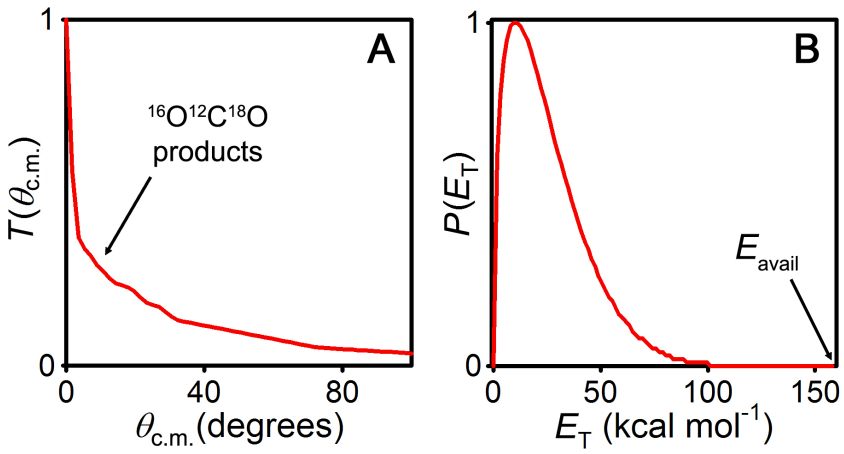

Figure 3.7: **Center-of-mass-frame (A) angular and (B) translational energy distributions from the $^{16}O_2$ + $^{12}C^{18}O_2$ oxygen isotope exchange reaction obtained from TOF fits of m/z = 46.** The peak of the distribution of available energies is E_{avail} = 158 kcal mol^{-1}. Only the experimentally accessible range of c.m. angles ($\theta_{c.m.} < 100°$) is shown.

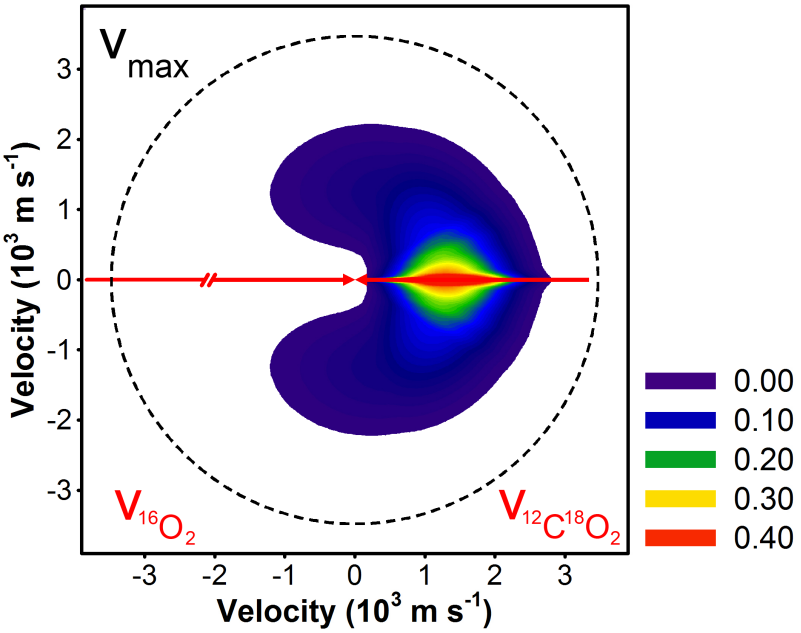

Figure 3.8: **Velocity-flux contour diagram for $^{16}O^{12}C^{18}O$ products of $^{16}O_2$ + $^{12}C^{18}O_2$ collisions in the center-of-mass frame.** The white arrows are the initial $^{16}O_2$ and $^{12}C^{18}O_2$ velocity vectors, and dashed white line is the maximum recoil velocity for $^{16}O^{12}C^{18}O$ (v_{max}). $^{16}O^{12}C^{18}O$ products are scattered opposite the initial direction of the $^{12}C^{18}O_2$ velocity vector.

The $^{16}O^{12}C^{18}O$ products scattered mainly in the forward direction ($\theta_{c.m.} = 0^\circ$), though there was significant sideways scattering. Experimental sensitivity in the backward direction was insufficient to detect backward-scattered $^{16}O^{12}C^{18}O$ products, so forward-backward symmetric scattering (i.e., evidence for a long-lived intermediate complex) could not be ruled out. At these collision energies, however, an intermediate is unlikely to survive for a rotational period. The average total translational energy distribution for the two products was 25 kcal mol^{-1}, or 16% of the available energy; the $P(E_T)$ distribution was peaked at E_T = 10 kcal mol^{-1}. We estimate the yield for reaction 3.2 to be $\leq$ 2% of all O_2–CO_2 collisions. This estimate is an upper limit because the complete Newton circle for inelastically scattered $^{16}O_2$ + $^{12}C^{18}O_2$ products was not observed in these experiments. Vibrational excitation of the O_2 may also be important in promoting reaction, but the vibrational temperature of O_2 present in the expanded plasma is unknown.

Our experimental results are consistent with a $^{16}O^{12}C^{18}O$ product that rebounds from the $^{12}C^{18}O_2$ reactant's initial direction after it collides with O_2; this mechanism is characteristic of reactions with substantial activation energies that require high collision energies. The highly peaked angular distribution is consistent with a direct mechanism or a very short-lived intermediate, but more surprising is the substantial internal energy of the products, which is much greater than that found for similar oxygen isotope exchange reactions between O(^3P) + CO, O(^1D) + CO_2, and O + O_2 [*Brunsvold et al.*, 2008; *Perri et al.*, 2004; *Van Wyngarden et al.*, 2007]. This large translational-to-internal energy conversion suggests that the reaction proceeds through an intermediate species that facilitates efficient translational-to-internal energy transfer or through a non-adiabatic transition to another electronic surface.

On average, 134 kcal mol^{-1} of internal energy is available to both products. This excess energy could be distributed among the five vibrational and four rotational degrees of freedom in O_2 and CO_2. Alternatively, this energy could be in the form of electronically excited products, including the $a^1\Delta_g$, $b^1\Sigma_g^+$, and $A^3\Sigma_u^+$ states of O_2, and the a^3A'' state of CO_2, which lies 119 kcal mol^{-1} above that for $CO_2(^1\Sigma_g^+)$ [*Braunstein and Duff*, 2000]. The mass-spectrometric detection, however, did not allow us to determine the electronic states

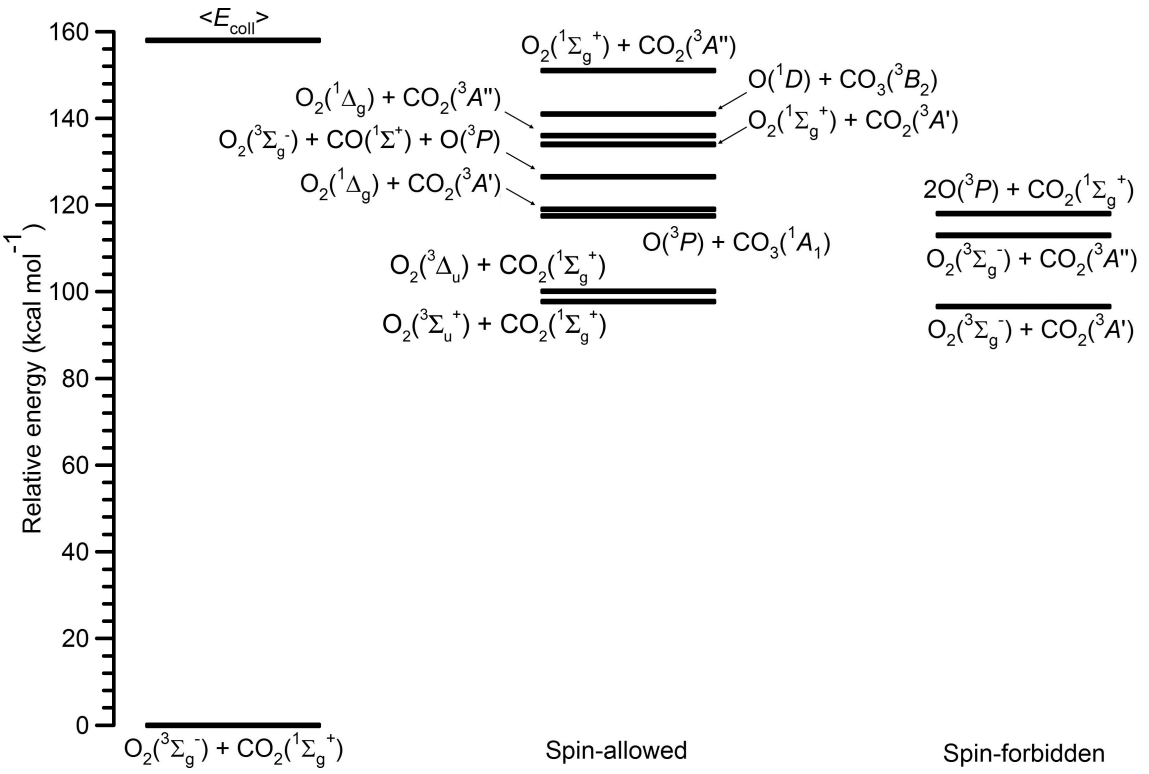

Figure 3.9: **Energetically allowed neutral product channels from O_2 + CO_2 collisions.** Energies are taken from the NIST Webbook [http://webbook.nist.gov], [*Mebel et al.*, 2004], and [*Braunstein and Duff*, 2000].

of the products.

Other reaction channels are possible (see Figure 3.9). We cannot rule out a CO_2 + O + O product channel because we did not collect sufficient data on the counter-fragment $^{18}O^{16}O$. However, the energetically allowed CO_2 + O(^3P) + O(^3P) channel (ΔH = 118 kcal mol^{-1}) is spin-forbidden, and spin conservation would instead favor O(^1D) + O(^3P) products, whose energetic threshold is 163 kcal mol^{-1} and above the average E_{avail} in the experiment. There is also sufficient energy to form O_3 + CO or O + CO_3 [*Mebel et al.*, 2004], and to dissociate CO_2 to form O_2 + O + CO, but because we were not anticipating these reactions, we did not search for the relevant detectable products.

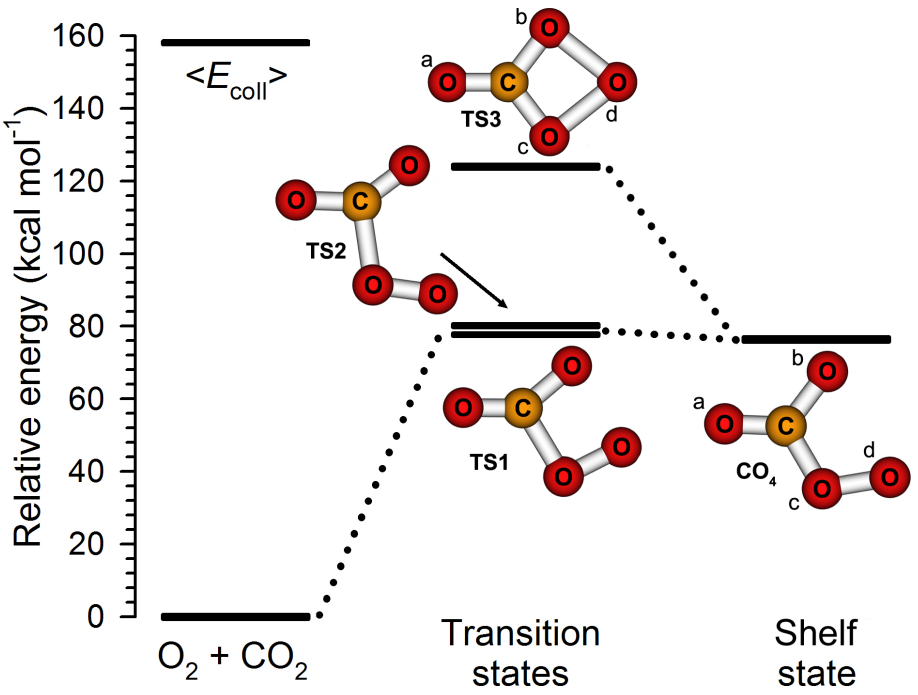

Figure 3.10: **Calculated energies and structures on the lowest triplet PES of O_2 + CO_2.** TS3 connects isoenergetic isomers of the CO_4 shelf.

3.4 Theoretical studies

To investigate whether an adiabatic mechanism exists for the O_2–CO_2 isotope exchange reaction, we performed *ab initio* calculations to find stationary points on the lowest triplet PES for O_2 + CO_2 reaction at the CCSD(T)/aug-cc-pVTZ level of theory using the MOLPRO electronic structure code [*Werner et al.*, 2006]. We identified two transition states (TS1 and TS2) connecting O_2 + CO_2 reactants with a triplet shelf state [$CO_4(^3A'')$; see Figure 3.10 and Table 3.1]. All three structures are planar. One atom of the oxygen molecule approaches the carbon atom of CO_2 and surmounts an activation barrier of 77.9 kcal mol^{-1} over TS1 to form a weak C–O bond and a $CO_4(^3A'')$ shelf (76.4 kcal mol^{-1}, just 1.5 kcal mol^{-1} below TS1) similar to a weakly bound CO_4 complex found at the B3LYP level of theory [*Cacace et al.*, 2003; *Elliott and Boldyrev*, 2005]. At 121.8 kcal mol^{-1}, we identified an effective transition state for $CO_4(^3A'')$ isomerization, TS3, containing a four-membered ring between the carbon atom and three oxygen atoms. A grid-based search revealed that TS3 is bound by 0.02 kcal mol^{-1} when zero-point energy is not considered, and that TS3

Table 3.1: Energies of stationary points associated with the exchange reaction $O_2 + CO_2 \rightarrow O_2 + CO_2$ on the lowest triplet potential energy surface*

	CO_4	TS1	TS2	TS3
$C_{HF}^{\dagger}$	0.973	0.977	0.969	0.945
ΔE [CCSD(T)/aug-cc-pVTZ]	76.0	77.9	80.0	120.9
$\Delta E_{ZPE}^{\ddagger}$ [CCSD(T)/aug-cc-pVTZ]	76.4	77.9	78.3	121.8
ΔE (CASPT2/cc-pVTZ)	91.2	95.6	97.1	137.4

*ΔE in kcal mol^{-1}.

†Coefficient of the Hartree-Fock configuration in the (8,10)-CASSCF expansion of the wave-functions.

‡ZPE-corrected. This calculation was not performed at the CASPT2 level of theory.

is connected to CO_4; a displacement in $O_d < 0.01$ Å towards CO_4 produced CO_4 upon geometry optimization. Thus, it acts as an 'effective' transition state for CO_4 isomerization; it resembles the bound $CO_4(^1A_1)$ structure lying 52.5 kcal mol^{-1} below it, although with a longer O_c–O_d bond length; both structures have C_{2v} symmetry [*Cacace et al.*, 2003; *Elliott and Boldyrev*, 2005; *Jamieson et al.*, 2007].

We observed some evidence for multi-reference character in CO_4. An additional bound state was found 0.8 kcal mol^{-1} above the energy of CO_4 at the MP2/cc-pVTZ level of theory, although it does not exist at the CCSD(T)/aug-cc-pVTZ level; the species is believed to be a resonance structure of $CO_4(^3A'')$. A spin contamination of $\langle S^2 - S_z^2 - S_z \rangle = 0.011$ in the region of the PES near TS3 also suggests some multi-reference character. Thus, CASPT2/cc-pVTZ calculations, which represent resonance qualitatively correctly and do not suffer from spin contamination, were performed to validate the CCSD(T) structures and energies. $CO_4(^3A'')$ was confirmed as a resonance hybrid of two bound-state structures, although the contribution from the single-reference structure to the resonance hybrid dominates the final geometry. The results of those calculations are summarized in Table 3.1 and Figure 3.11.

The uncertainty in the CCSD(T)/aug-cc-pVTZ energies is unknown, although a similar study in which the stationary points of the closely related $O(^3P) + CO_2$ system were characterized was recently completed (see Chapter 4). In addition to CCSD(T)/aug-cc-pVTZ simulations, W4 calculations (close to the full configuration-interaction and infinite-basis-set

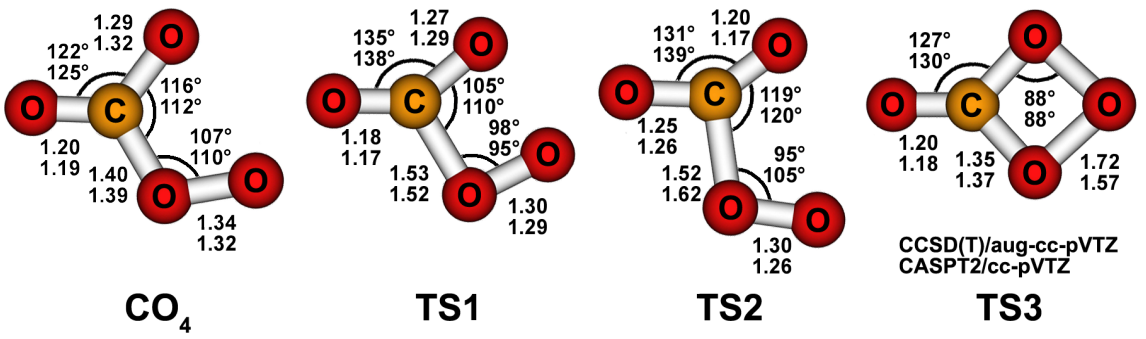

Figure 3.11: **Calculated stationary point geometries on the lowest triplet PES of CO_4.** CCSD(T)/aug-cc-pVTZ values (upper) and CASPT2/cc-pVTZ (lower) values are shown.

limits; see [*Karton et al.*, 2006]) were also performed, as they were found to be affordable, albeit marginally. The differences between the CCSD(T) and W4 results for the transition and bound states indicated a mean-unsigned error of 2.2 kcal mol^{-1}. We expect the errors in the analogous O_2 + CO_2 energies to be approximately the same.

3.5 Proposed mechanism

A possible pathway for oxygen isotope exchange occurs through the forward and reverse directions of the following three steps: O_2 + CO_2 → $[CO_4]^{‡}$ (TS1/TS2) → $CO_4(^3A'')$ → $[CO_4]^{‡}$ (TS3); see Figure 3.12. Spin-density maps (Figure 3.13) depicting the singly-occupied molecular orbitals (SOMOs) for CO_4 and TS3 are consistent with this mechanism. $CO_4(^3A'')$ is a diradical with unpaired electron density concentrated in *p*-type orbitals of the

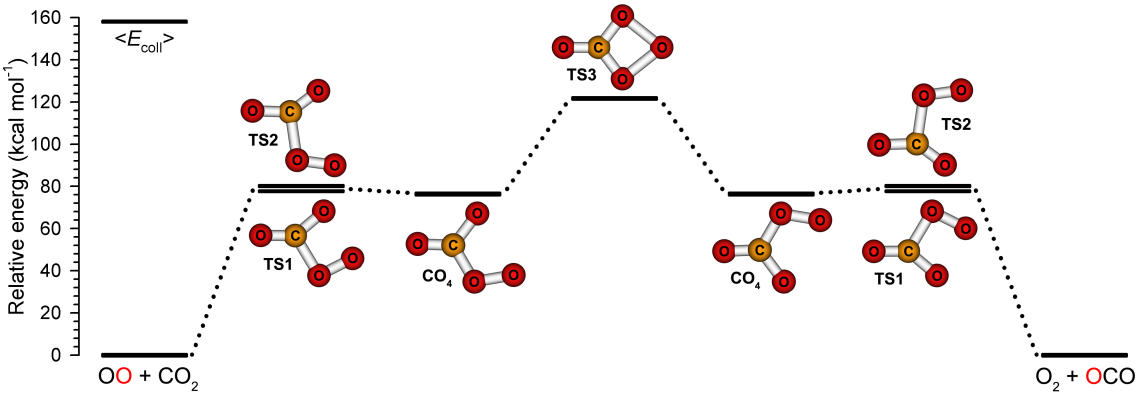

Figure 3.12: **Calculated energies and structures on the lowest triplet PES of O_2 + CO_2.** TS3 connects isoenergetic isomers of the CO_4 shelf.

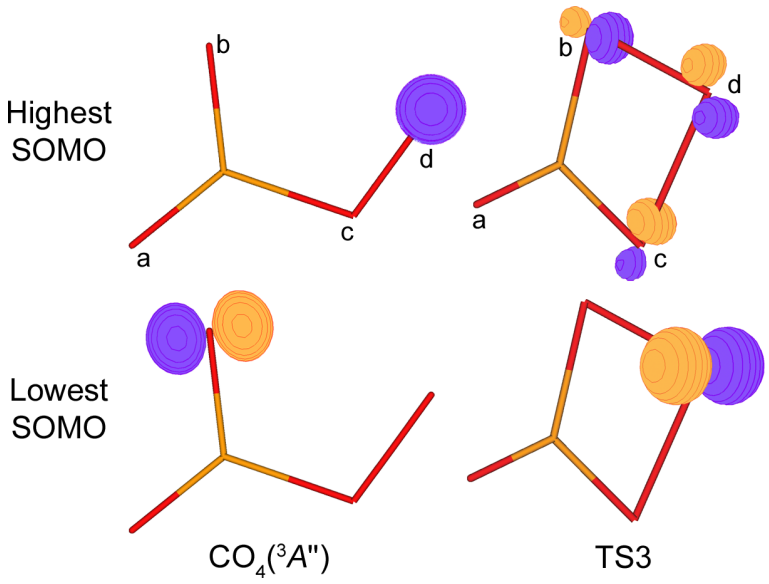

Figure 3.13: **Singly-occupied molecular orbitals (SOMOs) in the $CO_4(^3A'')$ and TS3 structures.** Surfaces containing 70% of the electron density are shown. Note that the highest SOMO of $CO_4(^3A'')$ and the lowest SOMO of TS3 have electron density primarily on O_d, suggesting the SOMO is a spectator during isomerization.

single-bonded oxygens, O_b and O_d. This spin density is consistent with the radical character expected for an association of the O_2 diradical with the carbon atom of CO_2, because the unpaired electrons in O_2 are in orthogonal π_g^* orbitals: As one C–O bond is formed between the in-plane π_g^* orbital of O_2 and the in-plane π_u^b orbital of CO_2 (the higher-energy π_g^{nb} orbital does not interact due to symmetry; see Figure 3.14), the out-of-plane π_g^* orbital on O_2 is a relative spectator to the O_2 radical addition. This interaction, along with the bending of the CO_2, produces the SOMOs for $CO_4(^3A'')$ shown in Figure 3.13. In TS3, the lowest SOMO contains localized electron density on O_d in an out-of-plane *p*-type orbital, suggesting that the unpaired electron on O_d continues to be a spectator during $CO_4(^3A'')$ isomerization. The highest SOMO, however, contains delocalized electron density, of anti-bonding (σ^*) character, in the plane of the molecule. This σ^* character may be interpreted as electron density taken from the lowest SOMO in $CO_4(^3A'')$ while being localized onto O_c during isomerization.

These theoretical results imply that an adiabatic mechanism exists for the oxygen isotope exchange reaction between O_2 and CO_2. During the isomerization of $CO_4(^3A'')$, the O_c–O_d σ-bond is cleaved homolytically (Figure 3.15): One electron moves to a *p*-type orbital on

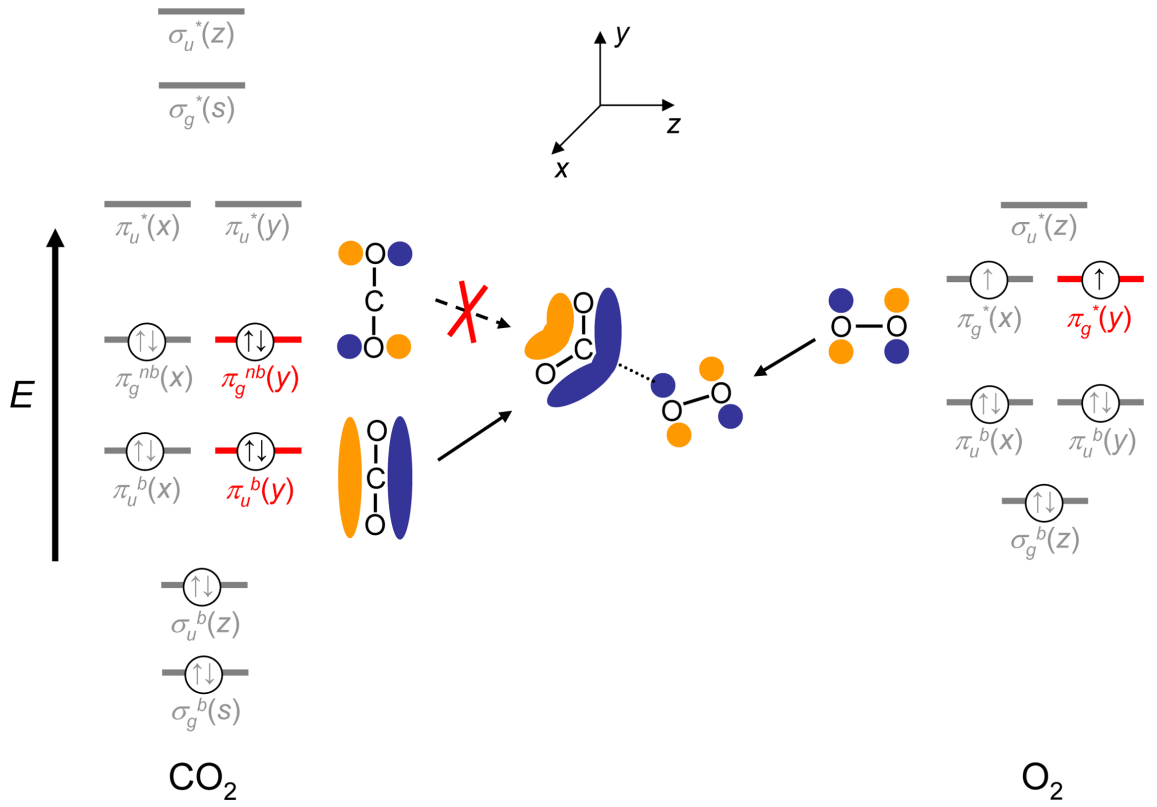

Figure 3.14: **Molecular orbital diagrams for O_2 and CO_2, adapted from *DeKock and Gray* [1980].** Sketches of the highlighted orbitals are shown. As O_2 collides with CO_2, it becomes stretched. In addition, CO_2 bends, increasing the energy of its doubly occupied, in-plane π-orbitals, π_u^b and π_g^{nb}. A weak interaction between the π_g^* orbital on O_2 and the π_u^b orbital on CO_2 is likely responsible for the small (1.5 kcal mol^{-1}) binding energy of CO_4. The π_g^{nb} orbital does not interact, to first approximation, due to symmetry.

O_c, while the other electron forms a bond with the unpaired electron on O_b. This pathway can account for the σ^* character of the highest-energy SOMO in TS3 (the O_b–O_d bond takes an electron from the O_c–O_d bond), and it preserves radical character on O_d. Thus, the $^3A''$ symmetry is preserved throughout the association, isomerization, and dissociation steps.

This mechanism is qualitatively consistent with the small reaction cross-section and a preference for rebounding reactive collisions inferred from the dynamics observed in the experiment. The O_2 must approach the CO_2 at very low impact parameters with high energies to overcome the initial barrier (TS1/TS2) and reach the 'shelf' of the bound $CO_4(^3A'')$. Momentum along the reaction coordinate beyond $CO_4(^3A'')$ with ~80 kcal mol^{-1} excess energy should further compress the C–O_c bond with synchronous bending of the C–O_c–O_d

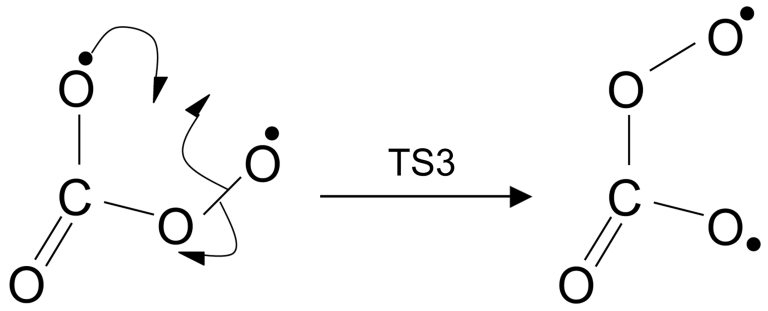

Figure 3.15: **Electron-pushing diagram of an adiabatic $CO_4(^3A'')$ isomerization through TS3.**

angle, stretching of O_c–O_d, and ring formation to form TS3, followed by rapid repulsion from the final TS1/TS2 state. Finally, the large change in geometry from reactants to TS3 should facilitate the transfer of some translational energy into internal degrees of freedom of the products. Reactive scattering should become less 'rebound'-like (forward-scattered) as E_{coll} is increased above the reactive threshold; at 37 kcal mol^{-1} above the reactive barrier, the tight transition state, repulsive exit channel leading out of TS1/TS2, and low angular momentum must limit the extent of sideways scattering. While some sideways scattering is indeed observed in the experiment, the E_{coll} dependence of $T(\theta_{\mathrm{c.m.}})$ is not known.

A non-adiabatic transition to another potential surface cannot be excluded, especially given the high internal energies observed in the products. At these high energies [80 kcal mol^{-1} above even the $CO_4(^3A'')$ shelf state], many excited-state surfaces must exist, and radiationless transitions via conical intersections may occur. While intersystem crossing (ISC) in the exit or entrance channels is unlikely at the high relative velocities of the experiment [*Landau*, 1932], spin transitions could readily occur if a complex is formed. For instance, the bridging oxygen atom in TS3, O_d, must be equivalently bound to O_b and O_c, and chemical intuition suggests that an intersection with a singlet surface may occur by spin-paired $CO_4(^1A_1)$ [*Cacace et al.*, 2003; *Elliott and Boldyrev*, 2005; *Jamieson et al.*, 2007].

3.6 Conclusion

An O_2–CO_2 isotope exchange reaction on the ground triplet electronic surface is possible and is consistent with our laboratory observations. Nevertheless, additional work would

be valuable in the confirmation of this hypothesis. Collision-energy-dependence studies of the product angular distribution may elucidate the mechanistic origins of the low average translational energy of products. Experimental detection of O_2 counter-fragments and a search for products from other channels (e.g., spectroscopic identification of electronically excited states) would also be revealing. Last, a more complete surface, reactive trajectories, and locations of possible surface intersection seams leading to ISC would be vital to a full explanation of the reaction dynamics.

3.7 Acknowledgements

We thank G. B. Ellison, S. L. Mielke, and J. E. Wulff for insightful discussions. This work was supported by the Missile Defense Agency under cooperative agreement HQ0006-05-2-0001. L. Y. Y. was supported by the Davidow Fund, and G. C. S. was supported by AFOSR grant FA955D-07-1-0095.

Appendices

3.A Non-reactive scattering of O_2 and CO_2

The experiment mainly observed signals due to $^{16}O_2$ scattered with little deflection from its initial direction (see Newton diagram in Figure 3.2); these signals corresponded to the sum of elastic and inelastic scattering collisions of $^{16}O_2$, which we could not resolve, so they will be referenced collectively as "scattered $^{16}O_2$." Five representative laboratory-frame TOF distributions (m/z = 32), the c.m. angular and translational energy distributions, and the laboratory-frame angular distribution obtained from $^{16}O_2$ product detection are shown in Figure 3.16. Scattered $^{16}O_2$ had 126.3 kcal mol^{-1} total translational energy, or 80% of the available energy, on average. The experimental translational energy distribution was peaked at ~148 kcal mol^{-1}. The c.m. angular distribution for ^{16}O was highly peaked in the forward direction with little scattered intensity for $\theta_{c.m.} > 30^\circ$; however, the velocity and angular range for $^{16}O_2$ product detection in the experiment prevented the detection of backward-scattered $^{16}O_2$ (see Figure 3.2). Some dependence of the c.m. translational energy distribution on the c.m. angular distribution was observed in the ^{16}O TOF data; the forward-convolution simulations became increasingly faster than the data at larger laboratory and c.m. angles (e.g, $\Theta = 18^\circ$, 28°, and 42° in Figure 3.16). We also note that, like for ^{16}O (see Sections 4.4.2.1 and 4.5.2), the c.m. angular distribution for inelastically scattered $^{16}O_2$ at $\theta_{c.m.} \sim 0^\circ$ is an extrapolation because of high background from the hyperthermal source at the small laboratory angles corresponding to small c.m. angles for $^{16}O_2$. Most of the $^{16}O_2$ probably scatters forward through high-impact-parameter collisions, but the limited constraints on the $\theta_{c.m.} \sim 0^\circ$ angular distribution (e.g., the laboratory-frame angular distribution, which only probes $\Theta = 6^\circ$) increase the uncertainty in that part of the c.m. angular distribution.

The experiment mainly observed $^{12}C^{18}O_2$ scattered opposite its initial direction in the c.m. frame (see Newton diagram in Figure 3.2). Detected $^{12}C^{18}O_2$ products (m/z = 48) showed best-fit c.m. translational energy distributions that were both broader and lower in energy, on average, than that obtained for forward-scattered $^{16}O_2$. A single pair of $P(E_T)$ and $T(\theta_{c.m.})$ distributions was not sufficient to describe the m/z = 48 TOF distributions (see Sections 4.4.2.1 and 4.5.2), and a second pair of $P(E_T)$ and $T(\theta_{c.m.})$ distributions was

included in the fit; five representative laboratory-frame TOF distributions, the c.m. angular and translational energy distributions, and the laboratory-frame angular distribution obtained from $^{12}C^{18}O_2$ product detection are shown in Figure 3.17, along with the c.m. velocity-flux diagram in Figure 3.18. The first $P(E_T)$ and $T(\theta_{c.m.})$ pair for inelastically scattered $^{12}C^{18}O_2$ described the scattering at $\theta_{c.m.} < 125^\circ$. In this region, the angular distribution was peaked near $\theta_{c.m.} = 60^\circ$, though the probability of scattered products was roughly constant for $0^\circ < \theta_{c.m.} < 40^\circ$. The probability of finding these products decayed steadily at $\theta_{c.m.} > 60^\circ$. The corresponding translational energy distribution was peaked at 60 kcal mol^{-1} with an average $\langle E_T \rangle = 62.8$ kcal mol^{-1}, or 40% the available energy. The second $P(E_T)$ and $T(\theta_{c.m.})$ pair for inelastically scattered $^{12}C^{18}O_2$ described the scattering at $60^\circ < \theta_{c.m.} < 125^\circ$ (corresponding to the maximum $\theta_{c.m.}$ observed in the experiment), although there was a small component $0^\circ < \theta_{c.m.} < 60^\circ$. This angular distribution overlapped, in the sideways-scattering region, with the first pair. For $\theta_{c.m.} > 60^\circ$ the distribution increased rapidly until it peaked near $\theta_{c.m.} = 120^\circ$ and decayed quickly at $\theta_{c.m.} > 120^\circ$. This part of the distribution, however, is uncertain because our experiment did not probe it directly. The translational energy distribution was peaked at 103 kcal mol^{-1} with an average $\langle E_T \rangle =$ 100.8 kcal mol^{-1}, or 64% the available energy.

The similarity in product c.m. angular and translational energy distributions in the O_2 + CO_2 system and the $O(^3P)$ + CO_2 system (see Sections 4.4.2.1 and 4.5.2) suggests that the collisional energy transfer mechanism is similar in both cases. *Ryali et al.* [1982] found that CO_2 collisions with N_2, O_2, and Ar near at high collision energies all had similar translational-to-vibrational energy transfer cross-sections for the excitation of $CO_2(\nu_3)$, so they suggested that energy transfer sampled the repulsive part of the intermolecular potential in all cases. Transfer of vibrational energy from O_2 to CO_2 cannot be ruled out in our experiments because we did not characterize the vibrational temperature of the hyperthermal O_2. Consequently, the similarity in inelastic scattering dynamics of $O(^3P)$ and O_2 collisions with CO_2 could also be coincidental.

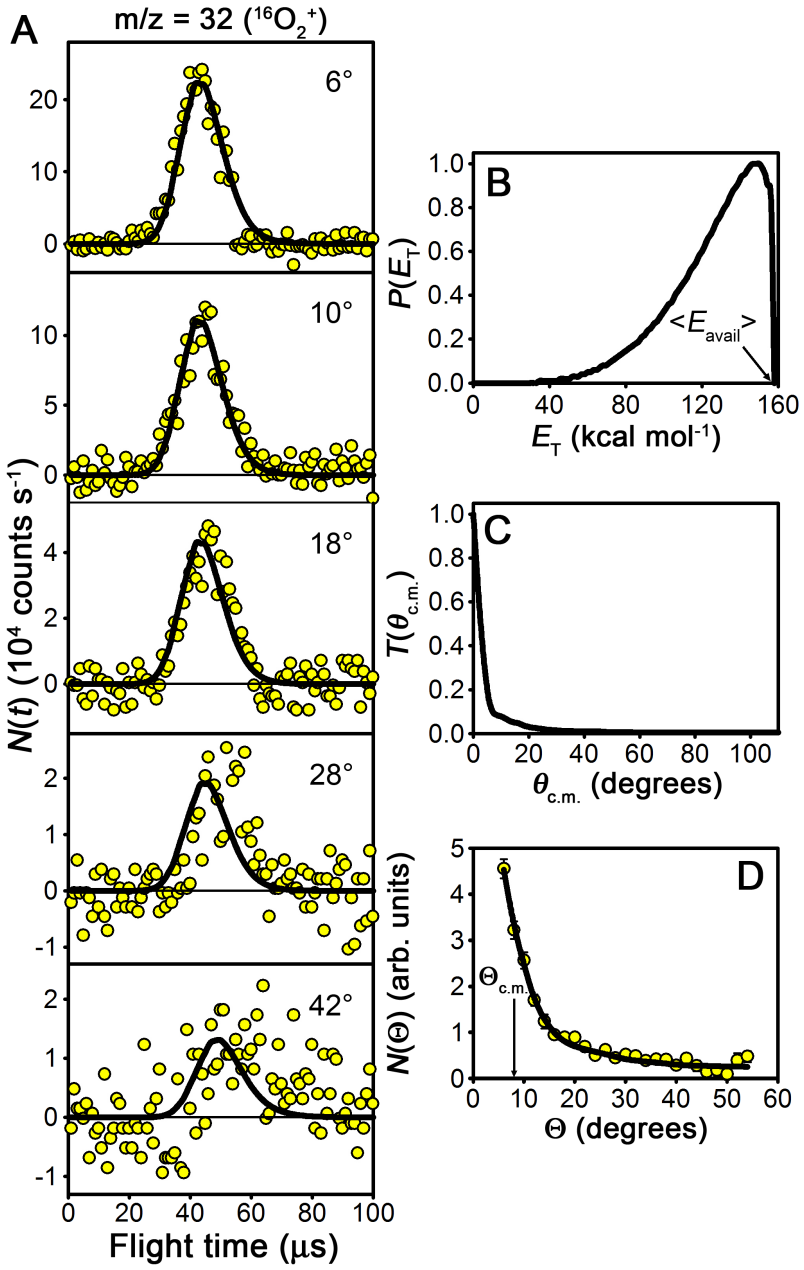

Figure 3.16: **Laboratory scattering data detected at *m/z* = 32.** (**A**) Laboratory TOF, (**B**) c.m. translational energy, and (**C**) c.m. and (**D**) laboratory angular distributions for scattered $^{16}O_2$ products from $^{16}O_2$ + $^{12}C^{18}O_2$ collisions at $\langle E_{coll} \rangle$ = 158.1 kcal mol^{-1}. The circles in (**A**) and (**D**) are experimental data, while the lines (orange and brown) are the best-fit forward-convolution simulations of the experimental data derived from the c.m. translational energy and angular distributions shown in (**B**) and (**C**), respectively. The error bars in (**D**) represent 2σ uncertainties in the integrated experimental TOF distributions (see Appendix 4.7). These data indicate that $^{16}O_2$ is scattered mainly in the forward direction with little change in its initial direction or velocity.

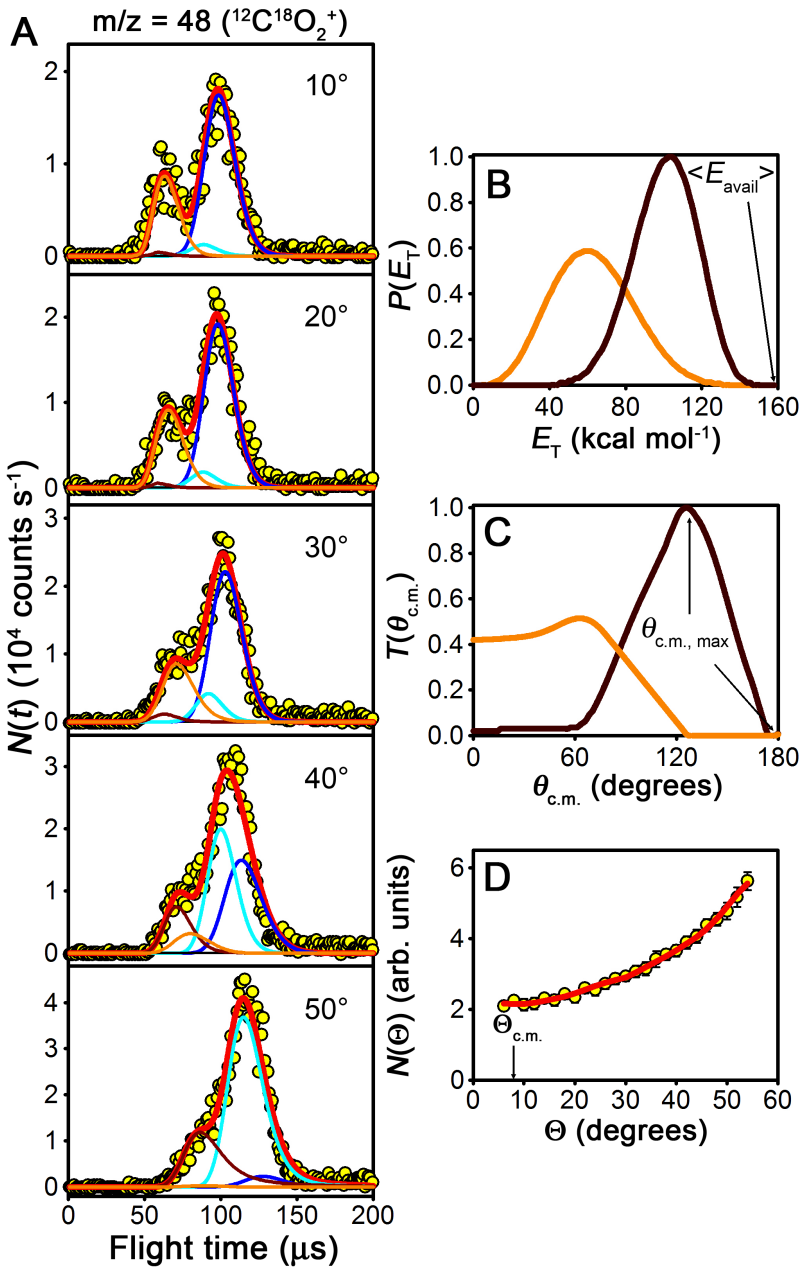

Figure 3.17: **Laboratory inelastic scattering data detected at *m/z* = 48.** (**A**) Laboratory TOF, (**B**) c.m. translational energy, and (**C**) c.m. and (**D**) laboratory angular distributions for inelastically scattered $^{12}C^{18}O_2$ products from $^{16}O_2$ + $^{12}C^{18}O_2$ collisions at $\langle E_{coll} \rangle$ = 158.1 kcal mol^{-1}. The circles in (**A**) and (**D**) are experimental data, while the lines are the best-fit forward-convolution simulations of the experimental data derived from the c.m. translational energy and angular distributions shown in (**B**) and (**C**), respectively. The error bars in (**D**) represent 2σ uncertainties in the integrated experimental TOF distributions (see Appendix 4.7). The dark blue and cyan lines correspond to products of $^{16}O(^3P)$ + $^{12}C^{18}O_2$ collisions, and they are discussed in Section 4.4.2.1. A single c.m. translational energy and angular distribution for each collision partner was insufficient to describe the TOF distributions of inelastically scattered $^{12}C^{18}O_2$, suggesting a scattering dependence on impact parameter.

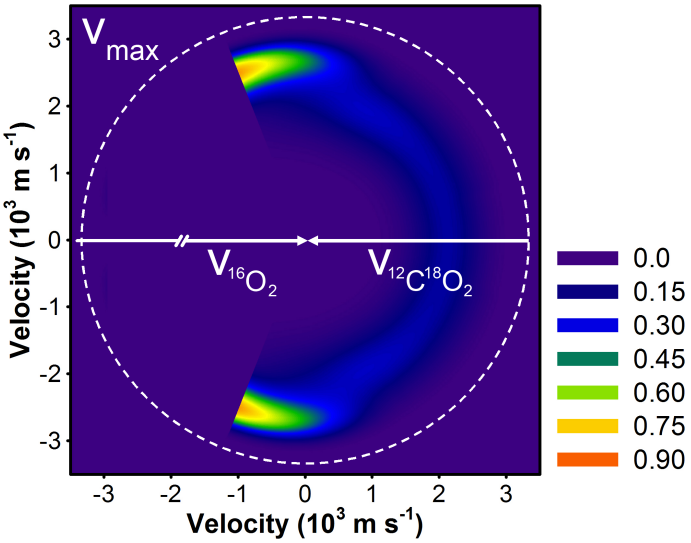

Figure 3.18: **Velocity-flux contour diagram for inelastically scattered $^{12}C^{18}O_2$ from $^{16}O_2$ + $^{12}C^{18}O_2$ collisions in the center-of-mass frame.** The white arrows are the initial $^{16}O_2$ and $^{12}C^{18}O_2$ velocity vectors and dashed white line is the maximum recoil velocity for $^{12}C^{18}O_2$ (v_{max}). Only the c.m. angles for which the experiment were sensitive are shown; inelastically scattered $^{12}C^{18}O_2$ from high-impact-parameter collisions are not shown, as their flux would be off-scale. Strong coupling of the $P(E_T)$ and $T(\theta_{c.m.})$ distributions was observed.

3.B MATLAB program for generating Newton diagrams

A series of programs (linked as functions) was written in MATLAB so meaningful Newton diagrams could be generated with little effort. This proved to be quite useful during data analysis because the program could display expected product times-of-flight, speeding up the forward-convolution fitting process considerably. The programs included here (*NewtonD.m*, *NewtonDcalc.m*, and *NewtonDplot.m*) use parameters specific to the MSU crossed-beam apparatus, but the code is general and the parameters adjustable for use with any crossed-beam apparatus with arbitrary crossing angle. Figure 3.19 shows a sample input and output.

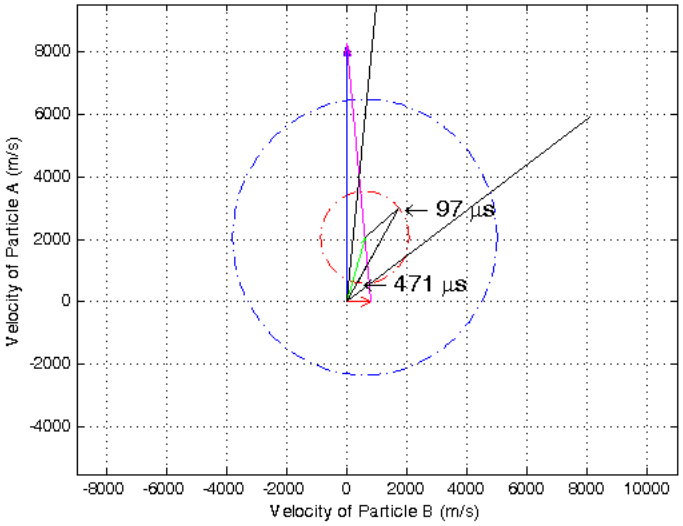


```
>> NewtonD(2,30)
Observed m/z
    48

Lab angle (degrees)
    30

Predicted center-of-mass angles (degrees)
   Fast channel | Slow channel
          124       -15.062
```

Figure 3.19: **Sample output of the *NewtonD.m* program.** Predicted c.m. angles are defined relative to the slow product's c.m. velocity vector.

3.B.1 NewtonD.m

```
% Program for generating Newton diagrams for molecular scattering.
% Command line input is NewtonD(observed,labangle)

function NewtonD(observed, labangle)
clear m1 m2 v1 v2 theta e DEint

observed=observed;     % observed product (1 or 2) as inputted below
labangle=labangle;     % lab angle of observation relative to initial v1
                       % vector, in degrees
```

```
% Begin input section

m1=16;      % mass of particle 1 in g/mol
v1=8262;    % initial velocity of particle 1 in m/s

m2=48;      % mass of particle 2 in g/mol
v2=800;     % initial velocity of particle 2 in m/s

theta=0.5;  % angle between v1 and v2 in pi radians, e.g. 0.5 --> 0.5*pi
            % = 90 degrees

e=0.5;      % elastic scattering efficiency 0 < e ≤ 1)
DEint=0;    % gain of internal energy upon reaction in kcal/mol

mp1=16;     % mass of product 1 in g/mol
mp2=48;     % mass of product 2 in g/mol

minangle=6;     % minimum lab angle relative to v1 vector, in degrees
maxangle=54;    % maximum lab angle relative to v1 vector, in degrees

length=33.66;   % distance between interaction region and ionizer in cm

if observed == 1
    IFT=0;2.44*sqrt(mp1);    % ion flight time (delay) in microseconds
else if observed == 2
        IFT=0;2.44*sqrt(mp2);
    end
end

delec=0;3;               % electronics delay in microseconds
dlaser=0;174;            % laser firing delay in microseconds
otravel=0;(0.99/v1)*10^6;       % O-atom travel time from nozzle to
                                % interaction region in microseconds

% End input section

% Input error check

if observed ≠ 1 && observed ≠ 2
    disp('Invalid input, "observed" must equal 1 or 2');
    return;
end

% Begin calculations

hold off
format short g

disp('Observed m/z');   % Display observed mass
if observed == 1
    disp(mp1);
else if observed == 2
        disp(mp2);
    end
end
disp('Lab angle (degrees)');
disp(labangle);
```

```
disp('Predicted center-of-mass angles (degrees)');
disp('   Fast channel | Slow channel');

% Iterate; first round includes specified change in internal energy,
% second round sets the internal energy change to zero, i.e.
% elastic scattering.
for i = 1:2
    [vc, thetavc, vrel, u1, u2, vrelp, up1, up2, Ecoll, phi, vd, chi]=
        NewtonDcalc(m1, m2, v1, v2, theta, e, DEint, mp1, mp2, labangle,
        observed);
    NewtonDplot(v1, v2, vc, thetavc, up1, up2, e, minangle, maxangle,
        labangle, vd, length, IFT, delec, dlaser, otravel, chi);
    if DEint == 0
        return;
    else
        DEint=0;
    end
end

disp('Collision Energy (kcal/mol)');
disp(Ecoll);
```

3.B.2 NewtonDcalc.m

```
% Function for calculating center-of-mass quantities

function [vc, thetavc, vrel, u1, u2, vrelp, up1, up2, Ecoll, phi, vd,
    chi]=NewtonDcalc(m1, m2, v1, v2, theta, e, DEint, mp1, mp2,
    labangle, observed)

% reactant parameters
mu=m1*m2/(m1+m2);                                   % reduced mass
vc=sqrt((m1/(m1+m2)*v1)^2+(m2/(m1+m2)*v2)^2);       % CM velocity
vrel=sqrt(v1^2+v2^2-2*v1*v2*cos(theta*pi));         % relative velocity
u1=m2/(m1+m2)*vrel;                                 % velocity of particle 1
                                                    % in CM frame
u2=m1/(m1+m2)*vrel;                                 % velocity of particle 2
                                                    % in CM frame
thetavc=asin((u2/vc)*(v1/vrel)*sin(theta*pi));      % angle between CM
                                                    % velocity and v2
Ecoll=(1/2)*mu/1000*vrel^2/4.184/1000;              % CM collision energy

% reactive product parameters
mup=mp1*mp2/(mp1+mp2);                              % reduced mass
vrelp=sqrt(((mu/1000)*vrel^2-2*(DEint*1000*4.184))/(mup/1000));
    %relative velocity
up1=mp2/(mp1+mp2)*vrelp;                            % velocity of product 1
                                                    % in CM frame
up2=mp1/(mp1+mp2)*vrelp;                            % velocity of product 2
                                                    % in CM frame

phi=labangle*pi/180-(theta*pi-(thetavc));           % angle between lab
                                                    % detection vector and
                                                    % CM velocity

% case structure determining output parameters
if observed == 1
```

```
    up=up1; u=u1; v=v1;
else if observed == 2
        up=up2; u=u2; v=v2;
    end
end

% product velocity in lab frame with case structure for removal of
% imaginary roots.

if imag(roots([1 -2*vc*cos(phi) vc^2-(up*sqrt(e))^2])) == 0
   vd=roots([1 -2*vc*cos(phi) vc^2-(up*sqrt(e))^2]);
   % Solve for product velocity observed at detector
   if vd(1) <= 0 && vd(2) <= 0
       vd(1)=0;
       vd(2)=0;
   else if vd(1) > 0 && vd(2) <= 0
           vd(2)=0;
       else if vd(1) < 0 && vd(2) > 0
               vd(1)=0;
           end
       end
   end

% Product scattering angle relative to CM velocity vector of reactant 2
   if phi > 0
       chi=(acos((diag(vd*vd')-vc^2-diag(up*up')*e)/(-2*vc*up*sqrt(e)))-
       asin(v2/u2*sin(thetavc)))*180/pi;
   else
       chi=360-(acos((diag(vd*vd')-vc^2-diag(up*up')*e)/(-2*vc*up*sqrt(e)))+
       asin(v2/u2*sin(thetavc)))*180/pi;
   end
   if imag(chi(1)) ~= 0
       chi(1) = 0;
   end
   if imag(chi(2)) ~= 0
       chi(2) = 0;
   end
   if chi(1) > 180
      chi(1)= chi(1)-360;
   end
   if chi(2) > 180
      chi(2)= chi(2)-360;
   end

% In case of imaginary roots
else
    vd(1,1)=10000;
    vd(2,1)=10000;
    chi=1;
    disp('         N/A         N/A')     % Display lack of solutions
end

%((1/2)*(mp1/1000)*(up1)^2*e)/4184       % CM Translational energy of
                                         % product 1
%((1/2)*(mp2/1000)*(up2)^2*e)/4184       % CM Translational energy of
                                         % product 2
```

3.B.3 NewtonDplot.m

```
function NewtonDplot(v1, v2, vc, thetavc, up1, up2, e, minangle,
    maxangle, labangle, vd, length, IFT, delec, dlaser, otravel, chi)

% Messy plotting code for pretty pictures

          x1 = vc*cos(thetavc);
          y1 = vc*sin(thetavc);
          N=256; t=(0:N)*2*pi/N;

plot(sqrt(e)*up2*cos(t)+x1, sqrt(e)*up2*sin(t)+y1, '-.r');
          % Newton circle for product 2
          hold on
          grid on

plot(sqrt(e)*up1*cos(t)+x1, sqrt(e)*up1*sin(t)+y1, '-.b');
          % Newton circle for product 1

legend('Particle 2', 'Particle 1')
% text(1,1,'Collision energy = \Ecoll kcal/mol')

          x0 = 0;
          y0 = 0;
          x1 = 0;
          y1 = v1;
plot([x0;x1],[y0;y1])    % Particle 1
          alpha = 0.05;  % Size of arrow head relative to the length of
                         % the vector
          beta = 0.2;    % Width of the base of the arrow head relative to
                         % the length
          hu = [x1-alpha*((x1-x0)+beta*((y1-y0)+eps)); x1; x1-alpha*
            ((x1-x0)-beta*((y1-y0)+eps))];
          hv = [y1-alpha*((y1-y0)-beta*((x1-x0)+eps)); y1; y1-alpha*
            ((y1-y0)+beta*((x1-x0)+eps))];
          plot(hu(:),hv(:))  % Plot arrow head

          x0 = 0;
          y0 = 0;
          x1 = v2;
          y1 = 0;
plot([x0;x1],[y0;y1],'r') % Particle 2
          alpha = 0.4;    % Size of arrow head relative to the length of
                          % the vector
          beta = 0.5;     % Width of the base of the arrow head relative to
                          % the length
          hu = [x1-alpha*((x1-x0)+beta*((y1-y0)+eps)); x1; x1-alpha*
            ((x1-x0)-beta*((y1-y0)+eps))];
          hv = [y1-alpha*((y1-y0)-beta*((x1-x0)+eps)); y1; y1-alpha*
            ((y1-y0)+beta*((x1-x0)+eps))];
          plot(hu(:),hv(:),'r')  % Plot arrow head

          x0 = v2;
          y0 = 0;
          x1 = 0;
          y1 = v1;
plot([x0;x1],[y0;y1],'m') % vrel
          alpha = 0.05;   % Size of arrow head relative to the length of
                          % the vector
          beta = 0.2;     % Width of the base of the arrow head relative to
```

```
                        % the length
          hu = [x1-alpha*((x1-x0)+beta*((y1-y0)+eps)); x1; x1-alpha*
            ((x1-x0)-beta*((y1-y0)+eps))];
          hv = [y1-alpha*((y1-y0)-beta*((x1-x0)+eps)); y1; y1-alpha*
            ((y1-y0)+beta*((x1-x0)+eps))];
          plot(hu(:),hv(:),'m')  % Plot arrow head

          x0 = 0;
          y0 = 0;
          x1 = vc*cos(thetavc);
          y1 = vc*sin(thetavc);
plot([x0;x1],[y0;y1],'g') % vc
          alpha = 0.1;    % Size of arrow head relative to the length of
                          % the vector
          beta = 0.25;    % Width of the base of the arrow head relative to
                          % the length
          hu = [x1-alpha*((x1-x0)+beta*((y1-y0)+eps)); x1; x1-alpha*
            ((x1-x0)-beta*((y1-y0)+eps))];
          hv = [y1-alpha*((y1-y0)-beta*((x1-x0)+eps)); y1; y1-alpha*
            ((y1-y0)+beta*((x1-x0)+eps))];
          plot(hu(:),hv(:),'g')  % Plot arrow head

          x1=10000*sin(minangle*pi/180);
          y1=10000*cos(minangle*pi/180);
plot([0;x1],[0;y1],'k')     % minimum lab angle

          x1=10000*sin(maxangle*pi/180);
          y1=10000*cos(maxangle*pi/180);
plot([0;x1],[0;y1],'k')     % maximum lab angle

if chi == 1
    return
else if chi ≠ 1
        x1=vd*sin(labangle*pi/180);
        y1=vd*cos(labangle*pi/180);
    plot([0;x1],[0;y1],'k')    % observed lab angle

        x0=vc*cos(thetavc);
        y0=vc*sin(thetavc);
        x1=vd*sin(labangle*pi/180);
        y1=vd*cos(labangle*pi/180);
    plot([x0;x1],[y0;y1],'k')  % center-of-mass scattering
    end
end

xlabel('Velocity of Particle B (m/s)')
ylabel('Velocity of Particle A (m/s)')
axis([-9000 11000 -5500 9500])

% Relevant quantities

disp(chi');

if vd(1) == 0 && vd (2) == 0
    TOF=[0 0];
else if vd(1) == 0
        TOF=[((length/100)/vd(1))*10^6 0];    % Predicted TOF times in
                                              % microseconds
```

```
    else if vd(2) == 0
           TOF=[((length/100)/vd(1))*10^6 0];  % Predicted TOF times in
                                               % microseconds
        else if vd(1) == 10000 && vd(2) == 10000
                TOF=[0 0];
            else if vd(1) > 0 && vd(2) > 0
                    % Predicted TOF times in microseconds
                    TOFfast=((length/100)/vd(1))*10^6;
                    TOFslow=((length/100)/vd(2))*10^6;
                    TOF=[TOFfast TOFslow];
                end
            end
        end
    end
end

% Display TOF on graph next to Newton circle
text(x1(1),y1(1),[' \leftarrow ',num2str(round(TOF(1)+IFT+delec+dlaser+
    otravel)), ' \mus'],'FontSize',14)

% Only display second TOF value if there is a product to display
if TOF(2) ~= 0
    text(x1(2),y1(2),[' \leftarrow ',num2str(round(TOF(2)+IFT+delec+
        dlaser+otravel)), ' \mus'],'FontSize',14)
else
    return
end
```